ADVANCED MATERIALS INTERFACES
Open Access
www.advmatinterfaces.de

A Modified Weber Number Capturing the Bouncing–Wetting Transition of Droplet Impact on Rough Surfaces

*Yanyao Bao, Zhongzheng Wang, Zhang Shi, and Yixiang Gan**

In this work, the effects of surface properties on bouncing–wetting transition of water droplet impacting rough surfaces in the Weber number (*We*) range from 18 to 221 are experimentally investigated. The correlation between impact outcomes and *We* is examined with an empirical function, and an impact outcome transition from bouncing to no bouncing is identified with the increase of *We*. The results suggest that a higher surface area ratio promotes the bouncing to no bouncing transition on sample surfaces used in this study. To quantify the effects of surface wetting area on the transitions of droplet impact regimes, a modified Weber number, *We, is proposed by taking the actual surface area into account. Results show that the regime transitions of droplet impact on samples of different surface area ratios can be unified by the *We**. This study reveals the significance of actual surface area and the resultant adhesion force on the droplet impact dynamics on random rough surfaces.**

1. Introduction

Impact dynamics of liquid droplet is of high significance to a variety of technological and scientific fields, such as spray coating,[1] inkjet printing,[2] deposition of pesticides,[3] and anti-icing applications.[4] Since the pioneering work of Worthington on rapid droplet impact,[5] the underlying dynamics of the interplay among liquid droplet, ambient gas, and substrate have been investigated by many researchers.[6–8] Experimental investigations of droplet impact on solid substrate revealed six identical modes, including deposition, partial bouncing, complete bouncing, receding breakup, prompt splash, and corona splash.[9] The outcome of droplet collision depends on various factors, such as droplet properties,[10] surface conditions,[11,12] ambient pressure,[13] and impacting angle and velocity.[14]

Dimensionless numbers are used to characterize the droplet impact dynamics, with Weber number ($We = \frac{\rho v^2 D}{\gamma}$), Reynolds number ($Re = \frac{\rho v D}{\mu}$), and Ohnesorge number ($Oh = \frac{\mu}{\sqrt{\rho D \gamma}}$) being the most widely used parameters (where ρ is the liquid density; v is the impact velocity; D is the droplet original diameter; γ is the surface tension, and μ is the liquid dynamic viscosity). In addition, the maximum spreading factor ($\beta = \frac{D_{max}}{D}$, where D_{max} is the maximum droplet diameter during spreading), defined as the ratio of the maximum diameter to the initial one, is another important parameter to quantify the droplet impinging process on solid substrate. The droplet maximum spreading factor can be predicted by estimating the inertial, viscous, and capillary forces at droplet-surface collision, and various models correlating β with *We*, *Re*, and *Oh* have been proposed under different impacting regimes.[15–17] For instance, in the viscous regime where the maximum spreading of a droplet is determined by the balance of kinetic energy and viscous dissipation, β can be described as: $\beta \propto Re^{1/5}$.[18] While in the inertial regime, the spreading factor is dominated by the balance of inertial and capillary force, and β follows a simplified relation of $\beta \propto We^{1/4}$ based on a mass conservation argument.[19]

In order to achieve high surface water-repellency, hydrophobic coating and roughness design are often applied.[12,20] However, surface water-repellency could be undermined when the Weber number of an impacting droplet exceeds a threshold, where the impact outcome transits from bouncing to wetting due to the Cassie–Wenzel transition.[21,22] The Cassie state refers to the scenario that air is trapped in the micro-structure beneath the droplet. For Wenzel state, the liquid penetrates the rough grooves, resulting in a fully wetted surface. The

Y. Bao, Y. Gan
School of Civil Engineering
The University of Sydney
Sydney, NSW 2006, Australia
E-mail: yixiang.gan@sydney.edu.au
Z. Wang
School of Mechanical
Medical and Process Engineering
Faculty of Engineering
Queensland University of Technology
Brisbane, QLD 4001, Australia
Z. Shi
School of Mechanical and Mining Engineering
The University of Queensland
Brisbane, QLD 4072, Australia
Y. Gan
The University of Sydney Nano Institute (Sydney Nano)
The University of Sydney
Sydney, NSW 2006, Australia

The ORCID identification number(s) for the author(s) of this article can be found under https://doi.org/10.1002/admi.202201873.

DOI: 10.1002/admi.202201873

bouncing–wetting transition is of particular importance to understand the liquid impact dynamics on rough hydrophobic surface. This transition has been extensively investigated through experimental studies, especially on manufactured patterned surfaces with micro-pillars, where the equilibrium contact angle of surface,[23] droplet impact velocity,[24,25] size and spacing of the pillar,[26,27] and surface temperature[28] are found to influence the droplet impact outcomes. A generalized transition criterion based on the force balance of water hammer pressure P_{WH}, dynamic pressure P_D, and capillary pressure P_C is proposed to account for the bouncing–wetting transition on micro-structured surfaces, and the liquid penetration typically occurs when wetting force (P_{WH} and P_D) is larger than anti-wetting force (P_C).[21,25–27,29] For example, Bartolo et al. presented a semi-quantitative model to characterize the bouncing–wetting transition of droplet impacting on solid substrate by considering the force balance of inertial and surface tension.[21] The model proposed two impalement scenarios, i.e., "touch down" and "sliding," and the results suggest that the transition arises when P_D is larger than P_C. Malla et al. investigated the effects of pitch size and *We* on the droplet impact dynamics. A critical *We* for wetting transition was calculated based on the force balance of P_{WH}, P_D, and P_C, with droplet depinning found to be the main mechanism of wetting transition.[26] Droplet impact on soft solids,[30] porous surface,[31] and surface with liquid film[32] were also examined, and the corresponding transition mechanisms were investigated.

Other than micro-pillared surfaces, the investigations of droplet impact on rough heterogeneous substrate have also attracted the rising attention of researchers. It has been suggested by several studies that increasing surface roughness promotes prompt splashing and suppresses corona splashing under various conditions.[33–35] Rioboo et al. and Range and Feuillebois observed that the prompt splashing of droplet was promoted by increasing the surface roughness amplitude.[9,36] Range and Feuillebois experimentally examined droplet impact outcomes considering various liquids and surfaces.[36] The results suggested a critical Weber number for droplet splashing by correlating the ratio of the droplet size to the surface roughness coefficient. Latka et al. demonstrated that surface roughness suppressed corona splashing and promoted prompt splashing, and prompt splashing on rough surfaces can be suppressed by decreasing the ambient pressure.[35] On the contrary, some studies argue that the length scale of surface roughness alone does not influence the splashing threshold.[18,37] Roisman et al. investigated droplet splashing on rough surface and porous surface.[18] The results revealed that the droplet splashing was not affected by absolute length scales of the substrate roughness such as average roughness amplitude, and the splashing threshold was mainly influenced by Weber number and roughness slope of the substrate. Quetzeri-Santiago et al. studied the surface roughness effects on droplet impact dynamics.[37] It was concluded that micrometer-scale roughness had little impact on the droplet spreading dynamics, and the droplet splashing behaviors were dominated by a combined effect of roughness ratio, dynamic contact angle, and splashing ratio.

In existing publications, tremendous efforts have been devoted to investigating the bouncing–wetting transition on patterned surfaces and the splashing threshold of impacting droplet on rough surfaces. However, discussions on the droplet bouncing–wetting transition behaviors on random rough surfaces are scarce. The bouncing–wetting transition criterion based on wetting and non-wetting force balance analysis only apply to micro-structured surfaces, and it is challenging to understand the transition behaviors of droplet colliding with heterogeneous rough surfaces, i.e., engineered and natural surfaces with random roughness features.

In this work, we experimentally study the droplet impact dynamics and bouncing–wetting transition on random rough surfaces with various surface properties. The surfaces are characterized in terms of surface area ratio, RMS roughness, roughness slope, and fractal dimension calculated using Triangulation and Cube methods. The droplet impact outcomes covering a wide Weber number range from 18 to 221 are presented and categorized based on the droplet morphological evolution. The correlation between the droplet maximum spreading factor and We/Re is analysed. We further aim to understand the influence of surface properties on the droplet impact modes in the bouncing–wetting transitional region. The empirical logistic function is employed to evaluate the dependence of bouncing-no bouncing transition on *We* and surface properties. The effects of surface area ratio on each category of droplet impact outcomes are discussed, and a modified Weber number that incorporates a combined effect of droplet kinetic energy, surface energy, as well as droplet adhesion force is proposed to highlight the significance of the actual wetted area for the droplet impact dynamics.

2. Experimental Section and Sample Characterization

Deionized water drops were dispensed on the sample surface with experimental setup as shown in **Figure 1**. The setup consists of a high-speed CCD camera (Photron FASTCAM SA5), a 100 mm lens (VENUS LAOWA with 2× magnification), a single channel syringe pump (Suzhou Zede), an 18-gauge steel blunt needle, and an external LED light source. Surface samples are 5 different types of hydrophobic PTFE membrane filters purchased from Sterlitech, named as surface #1 to #5, and used as received. The sample was placed on the central region of an adjustable stage in which the height can be altered in the vertical direction.

During experiments, deionized water was pushed through the syringe pump to the vertically suspended needle, and the microliter water droplet was generated at the tip of needle. The water droplet detached from the needle tip due to gravity and then impacted the sample surface vertically. The diameter of the detached droplet was calculated as 3.2 ± 0.03 mm by controlling the flow rate and detaching interval. The droplet impact velocities ranging from 0.63 to 2.21 m s^{-1} were achieved by adjusting the height of needle stage. The sample surface was cleaned each time after the droplet impact and dried completely using an air pump before next impact. The droplet impact images were captured at framerate of 3000 s^{-1} and the captured images have a spatial resolution of 20 μm per pixel. The static contact angle was measured by placing the droplet gently on

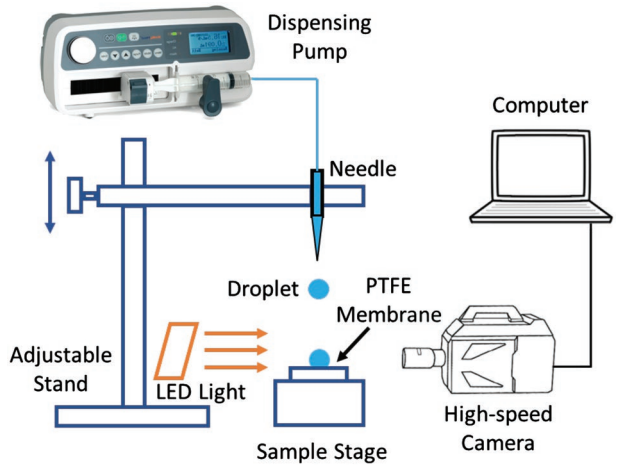

Figure 1. Schematic of the droplet impact experiment setup.

the sample surface, and 5 measurements were conducted for each type of sample surfaces. The static advancing contact angle (θ_a) of the PTFE membrane samples was measured with the syringe-needle method. The needle was placed 2 mm above the substrate, and the liquid was injected from the syringe needle with flow rate of 2 mL min^{-1}. The static advancing contact angle was obtained as droplet expanding on the substrate with stable expansion rate, and 5 measurements were conducted for each sample. The static contact angle θ_s and static advancing contact angle θ_a for all five types of samples are listed in **Table 1**. The results show no significant difference between the measured contact angles across the five rough surfaces adopted in this study. Note that though surfaces #1–#5 have manufactured pore size from 0.2 to 10 µm, these samples have been tested impermeable for the deionised water used in this work.

Figure 2 shows surface and 3D topographic images for sample #2 and #4, as an example. The surface images were captured using 3D digital microscopy Hirox HRX-01 with MXB-2500REZ lens at magnification of 500. 3D topographic images were acquired from the LEXT OLS5100 3D Laser Scanning Microscope. As the interaction between liquid droplet and solid substrate is significantly influenced by the surface morphology, the following surface topological parameters are characterized, including (1) surface area ratio (A_{ratio}); (2) RMS roughness (R_q); (3) RMS slope (R_s); (4) Fractal dimension (D_f). Here, A_{ratio} is defined as the ratio of actual surface area (A_s) to the projected area (A_p), i.e., $A_{ratio} = \frac{A_s}{A_p}$. The actual surface area can be larger than the projected surface area, due to the heterogeneity and roughness nature of sample surfaces. Therefore, A_{ratio} serves as an important parameter to quantify the contact and adhesion phenomena between droplet and varied surface samples. RMS roughness is often considered to describe the roughness feature of the surface, and RMS slope can be used as a higher order surface descriptor to characterize surface in terms of optical and tribological properties.[38,39] In addition, the fractal dimension has been successfully employed to quantify rough surface features across a wide range of length scales.[40,41] The values of measured surface properties are listed in **Table 2**, where 8 measurements were conducted for each surface type. Sample #1 and #2 have A_{ratio} of around 1.04, and A_{ratio} ranges between 1.1 and 1.12 for sample #3, #4, and #5. For the RMS roughness, sample #1 and #2 have a lower value compared to sample #3, #4, and #5. All five types of samples have similar level of RMS slope and fractal dimension, though sample #1 and #2 have larger fluctuation for RMS slope. In addition, there is no significant difference observed for all five samples in terms of roughness kurtosis and roughness skewness.

Table 1. Static contact angle and advancing contact angle for all sample surfaces.

Sample surface type	Static contact angle, θ_s [°]	Static advancing contact angle, θ_a [°]
#1	134.5 ± 1.8	149.3 ± 2.1
#2	134.4 ± 2.9	154.1 ± 1.7
#3	134.4 ± 2.2	153.4 ± 1.4
#4	137.2 ± 1.9	148.0 ± 2.2
#5	137.7 ± 1.6	151.6 ± 1.9

The impact velocities, v, and non-dimensional numbers, We, Re, and Oh, used for droplet impact experiments are listed in **Table 3**. For each We, 32 experiments are conducted for sample #2 and #4 due to the distinct surface properties in surface area ratio and RMS roughness. Additional 32 sets of experiments are conducted at We = 109, 131, 152, and 174 for sample #1, #3, and #5 to further evaluate the droplet bouncing–wetting transition behaviors.

3. Results and Discussions

3.1. Droplet Impact Modes

Six droplet impact modes were identified from the experimental observations at different Weber numbers, including splitting–bouncing, bouncing–splitting, complete bouncing, partial bouncing, no bouncing, and receding breakup. **Figure 3** shows the temporal evolution of water droplet impacting on PTFE membrane sample #4 with different outcomes presented. The difference between splitting–bouncing and bouncing–splitting lies in the occurrence sequence of splitting or bouncing during the impact. At relatively low We (e.g., We = 44), the splitting of droplet was observed before the droplet fully bounced from the substrate. With the increase of We (e.g., We = 109), the droplet first fully bounces from the substrate, then splits into two or more isolated droplets during the lifting process. Partial bouncing refers to the scenario that part of the droplet separates from the initial droplet at the time of impact, while the bottom part of the separated droplet remains on the substrate during the whole impacting process. The complete bouncing and no bouncing scenarios describe the impact outcomes that the droplet either totally bounces from the surface or sticks on the substrate after collision with the sample surface. The receding breakup occurs at relatively high We ($We \geq 131$), where the droplet breaks into several parts during the retracting stage due to the reduced contact angle of lamella region. The Supporting Information contains the videos showing these typical impact modes. It should be noted that the different outcomes presented here are selected from 5 different We,

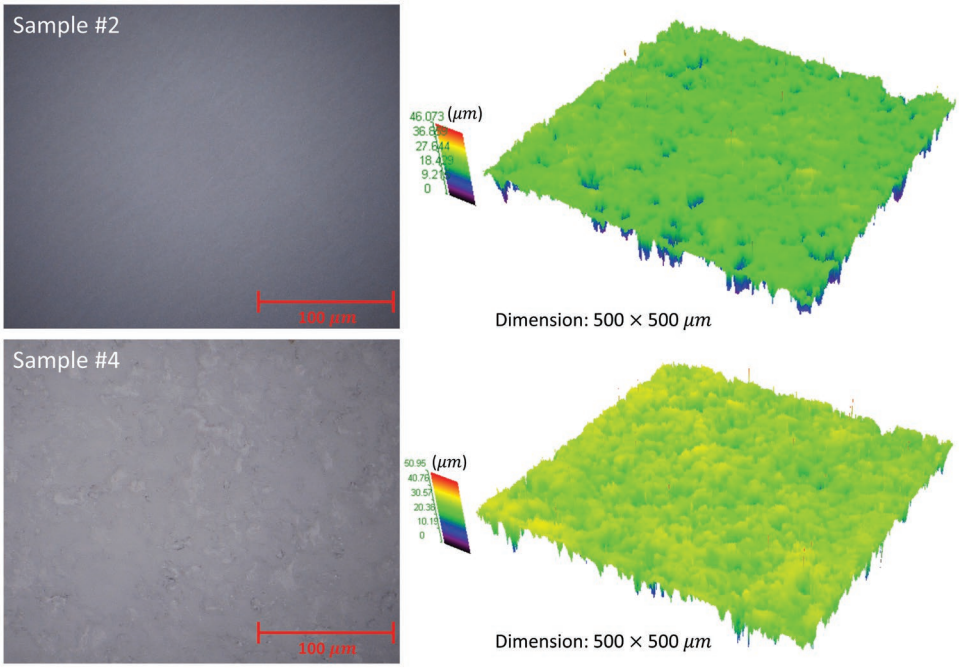

Figure 2. Surface image and microscopic 3D scan of sample surface #2 and #4.

while the same impact outcome can be observed on different samples under varied *We* close to the transition regime between modes. More details are discussed in Section 3.3.

3.2. Maximum Spreading Factor β as Function of *We* and *Re*

The correlation between the maximum spreading factor β and dimensionless number *We* and *Re* is examined in this section. As the droplet contacts the substrate, the droplet diameter is found to increase as the increase of impact velocity. The maximum diameter of a droplet is measured by identifying the maximum droplet expansion during the impact process through image processing. Spreading factor at *We* ranging from 18 to 174 can then be analyzed. The droplet breaks up before reaching the maximum spreading when *We* is higher than 174. The maximum spreading factor as function of *We* and *Re* for all five sample surfaces are presented in **Figure 4**. The correlation between β and *We* is calculated as $\beta = 0.58We^{0.37}$, and the correlation for β and *Re* is $\beta = 0.006Re^{0.73}$. The derived correlation between β and *We* is comparable to the result reported in Huang's work where $\beta = 0.47We^{0.4}$.[42] The results suggest that the kinetic energy of the impinging droplet on sample surfaces is consumed by droplet surface energy as well as viscous dissipation at the shear boundary layer. It is also observed that the maximum spreading factor is similar for all surfaces at the same *We*, suggesting that β is not noticeably influenced by surface area ratio and RMS roughness in the reported value range. The relation between droplet maximum spreading factor β and $ReWe^{1/2}$ is also examined, where a correlation of $\beta = 0.06Re(We^{1/2})^{0.37}$ is identified for all five different samples surfaces. The results suggest that the spreading factor is dominated by the kinetic energy and insensitive to the surface properties. On the other words, the observed different impact outcomes are likely the results of droplet retracting and detaching stages.

3.3. Bouncing–Wetting Transition

In this section, the effects of surface topological parameters on the bouncing–wetting transition are investigated. For the con-

Table 2. Surface properties for 5 different samples.

Sample	Surface area/projected area	RMS roughness R_q [μm]	RMS slope R_s	Roughness kurtosis [R_{ku}]	Roughness skewness [R_{sk}]	Fractal dimension D_{f1} (triangulation)	Fractal dimension D_{f2} [cube]
#1	1.037 ± 0.0241	19.207 ± 2.934	0.153 ± 0.0322	5.69 ± 0.148	−1.471 ± 0.014	2.155 ± 0.0126	2.0962 ± 0.00692
#2	1.041 ± 0.0235	20.457 ± 2.881	0.152 ± 0.0354	5.72 ± 0.181	−1.423 ± 0.022	2.155 ± 0.0239	2.0997 ± 0.0134
#3	1.104 ± 0.0369	24.862 ± 2.190	0.162 ± 0.0233	5.83 ± 0.166	−1.516 ± 0.031	2.144 ± 0.0217	2.0916 ± 0.00957
#4	1.114 ± 0.0171	24.157 ± 1.802	0.166 ± 0.0156	5.71 ± 0.151	−1.522 ± 0.017	2.146 ± 0.0168	2.0919 ± 0.00798
#5	1.120 ± 0.0246	23.321 ± 2.600	0.157 ± 0.0114	5.87 ± 0.156	−1.453 ± 0.028	2.146 ± 0.0170	2.0955 ± 0.0069

Table 3. Droplet impact velocity, *We*, *Re*, and *Oh* employed in experiments.

Impact speed, v [m s^{-1}]	Weber number, *We*	Reynolds number, *Re*	Ohnesorge number, *Oh*
0.63	18	2004	
0.99	44	3168	
1.40	87	4480	
1.57	109[a)]	5009	
1.64	120	5248	
1.71	131[a)]	5487	0.0021
1.79	142	5728	
1.85	152[a)]	5926	
1.92	163	6144	
1.98	174[a)]	6336	
2.21	218	7084	

[a)]32 sets of experiments only conducted on sample #1, #3, and #5 at *We* = 109, 131, 152, and 174.

venience of discussing different impact outcomes mentioned above, the bouncing–splitting and splitting–bouncing scenarios are incorporated into the complete bouncing category, as the droplet is totally lifted up during the impact process regardless of the droplet being a complete one or separating into a few parts. As a result, the above-mentioned six impact outcomes regrouped into four impact outcomes, including complete bouncing, partial bouncing, no bouncing, and receding breakup. For 18 ≤ *We* ≤ 109, the droplet impact outcomes for all cases are complete bouncing. It is expected that no-bouncing will occur due to smaller kinetic energy at even lower *We*, as observed in previous studies.[43,44] For *We* ≥ 174, all the droplet impact outcomes are receding breakup. The droplet impact outcomes are dominated by *We* at low and high Weber number range despite of the heterogeneity of rough surfaces. The droplet bouncing–wetting transition behaviours in the *We* range from 109 to 174 are mainly discussed, and the occurrence proportion for all droplet impact outcomes is presented in **Figure 5**. Occurrence proportion is defined as the ratio of counts in a single outcome category to the total case number (32).

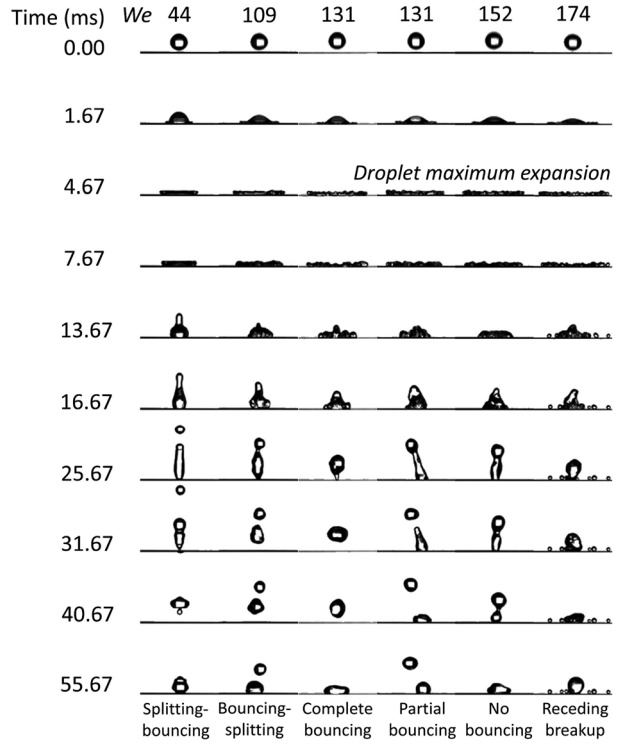

Figure 3. Droplet impact modes on PTFE membrane sample #4 at varied *We*.

A transition from bouncing to no bouncing is observed on both sample #2 and #4, where the droplet becomes less likely to completely bounce off from the substrate as *We* increases. In this transition regime, the complete bouncing and partial bouncing are perceived as bouncing category where droplet bouncing is identified, and no bouncing and receding breakup are considered as no bouncing category as the whole droplet stick on the substrate surface during the impact process. **Figure 6**a describes the bouncing to no bouncing transition on surface sample #2 and #4. The results suggest that the occurrence of bouncing decreases with the increase of *We*, and the occurrence of no bouncing increases with the increase of *We* for both surfaces. The correlation between bouncing/no bouncing outcome and *We* is analysed empirically by the logistic function:

$$\varphi = \begin{cases} 1 - \dfrac{1}{1 - e^{-k(We - We_c)}} (\text{bouncing}) \\ \dfrac{1}{1 - e^{-k(We - We_c)}} (\text{no bouncing}) \end{cases} \quad (1)$$

where φ is the occurrence proportion; We_c is the *We* value at the sigmoid's midpoint that leading $\varphi = 0.5$; k is the steepness of the fitted curve representing the logistic growth rate. The goodness-of-fit for the logistic function on outcome data points is evaluated by R^2, the coefficient of determination. It should be noted We_c is an estimated value from data interpolation to characterise the bouncing to no bouncing transition. It is observed that the occurrence of both bouncing and no bouncing outcomes in Figure 6a can be described by the logistic function with $R^2 > 0.97$, which shows a solid monotonic relation between impact outcomes and *We*. The steepness of transition is similar for sample #2 ($k = 0.144$) and #4 ($k = 0.115$). In addition, a second transition regime from complete bouncing to partial bouncing is identified, as shown in Figure 6b. For surface sample #2 and #4, the occurrence of complete bouncing decreases with the increase of *We* with $R^2 > 0.97$, showing a high correlation between the occurrence proportion of complete bouncing and *We*. The occurrence of partial bouncing first increases with the increase of *We*, then decreases with the increase of *We* when *We* is higher than 142 for sample #2 and 152 for sample #4. The non-monotonic trend of partial bouncing occurrence arises from the transition of partial bouncing to no bouncing or receding breakup when *We* is higher than 142 (for sample #2) or 152 (for sample #4).

The above-mentioned two regimes describe the droplet impact outcome transition from bouncing to wetting with the increase of *We*, and we firstly attempt to understand the

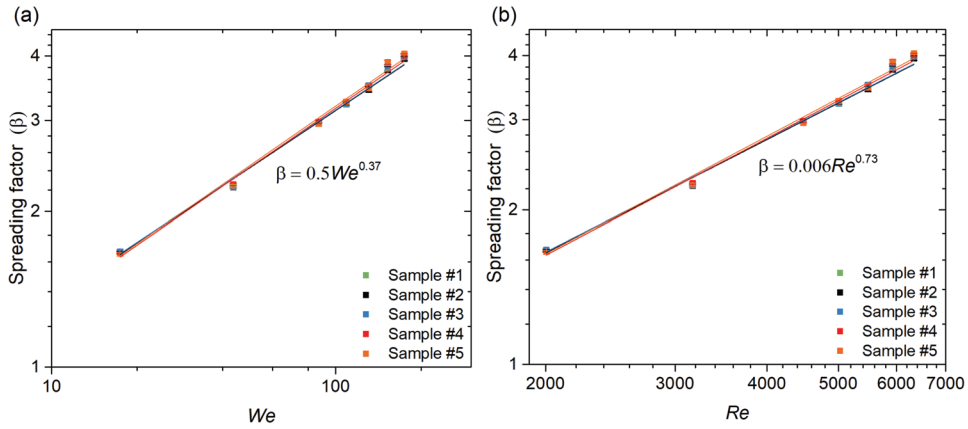

Figure 4. Spreading factor as function of a) *We* and b) *Re*.

transition mechanism based on contact angle hysteresis effects of the impacting droplet. The contact angle hysteresis and contact line speed play a significant role in understanding the droplet impact dynamics on heterogeneous surface.[45–48] The dynamic contact angle θ and the non-dimensional contact line speed $v^*$of an impacting droplet are presented as function of the non-dimensional time t^* at $We = 18$, as shown in **Figure 7**a,b. Here, v^* is characterised as the ratio between the contact line speed v_c and non-dimensional factor $(\rho D^3/\gamma)^{1/2}$, and t^* is defined as $(t - t_o)/T$, where t, t_o, and T refers to the current, initial, and total duration of contact line moving on the substrate, respectively. The contact angle and contact line speed are averaged value based on 5 measurements on each sample surface. The results suggest that the effects of contact angle hysteresis are neglectable, as both samples have similar contact angle and contact line moving speed during the droplet impact process. It should be noted that fingering instabilities have been observed for cases with $We > 100$, departing from the axisymmetric condition for image processing.[49] Therefore, the contact angle and contact line speed of an impacting droplet is only derived at $We = 18$ in this work to access the information of contact angle hysteresis and contact line speed.

Since the contact angle hysteresis effects have neglectable effects on the bouncing to no bouncing transition, another approach to illustrating the underlying mechanism for the transition phenomenon arises from the perspective of energy transfer, i.e., kinetic energy to surface energy. With the increase of *We*, more kinetic energy can be potentially converted to the surface energy during spreading, leading to an increased maximum spreading factor of the impacting droplet. Therefore, the contact area between the droplet and substrate during the impact process also increases with *We*, which further results in the increase of adhesion force between substrate and droplet. When the droplet kinetic energy for bouncing is consumed by the surface energy to the degree below detaching threshold, the impact outcome transition from bouncing to wetting is observed.

In the following, the correlation between surface properties and droplet impact outcomes is examined. The bouncing–wetting transition is mainly attributed to the increased adhesion force between the droplet and substrate, where the adhesion force is further affected by the droplet contact area on the substrate. Weber number relates the inertial force to the surface tension force, and the transfer from kinetic energy to surface energy during the impact process is described by *We*. However, the original *We* does not account for the effects of actual wetted surface area when a droplet collides with rough heterogeneous surfaces. For sample #2 and #4, there is no difference in the apparent wetted area as the maximum spreading factor is identical at the same *We*, as shown in Figure 4, while the

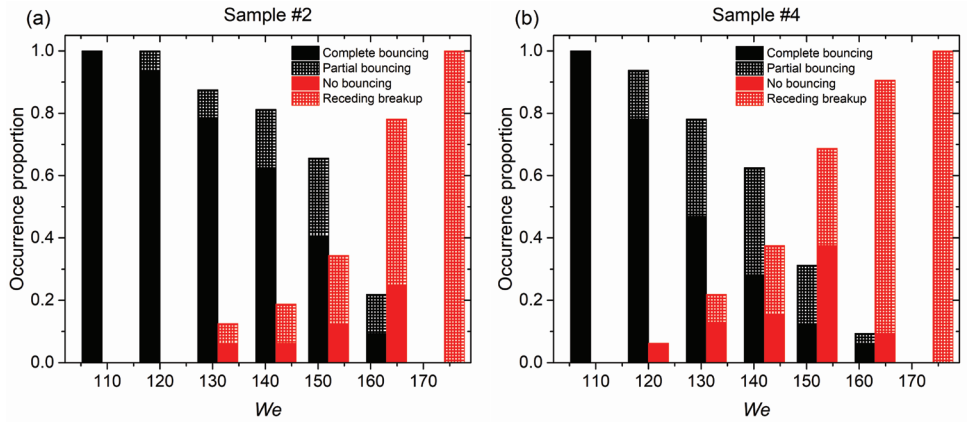

Figure 5. Droplet impact outcomes on PTFE membrane sample #2 and #4.

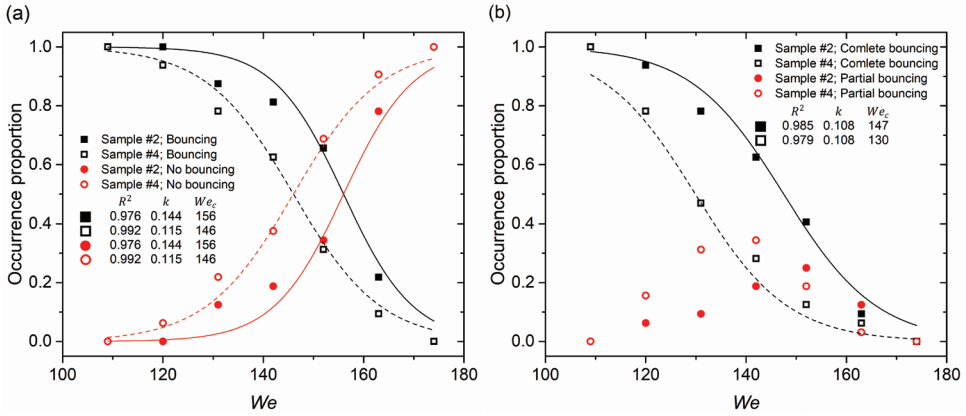

Figure 6. a) Occurrence proportion of bouncing and no bouncing outcomes for sample #2 and #4; b) Occurrence proportion of complete bouncing and partial bouncing outcomes for sample #2 and #4. The data points representing occurrence proportion are fitting by the logistic function, with fitting parameter (k, We_c) and coefficient of determination (R^2) provided.

occurrence proportion in the same impact outcome category is different. We propose the difference in the impact outcome stems from actual wetted surface area that significantly influences the adhesion between droplet and substrate. Therefore, to quantify the bouncing–wetting transition mechanism on samples with different surface area ratios, a modified Weber number (We^*) can be proposed by multiplying the original Weber number to the surface area ratio of the sample surface in the form as:

$$We^* = We \times A_{\text{ratio}} = \frac{\rho v^2 D}{\gamma} \times \frac{A_s}{A_p} \tag{2}$$

We^* considers the combined effects of inertial force, surface tension force, and adhesion force. In **Figure 8**, the droplet impact outcomes in the range of $109 \leq We \leq 174$ are plotted as function of We^*, and the resulted We^* ranges from 113 to 181 for sample #2, and 121 to 193 for sample #4. The logistic function is applied to correlate the occurrence proportion with We^* in each outcome category except for partial bouncing. It is observed that the outcome occurrence of bouncing, no bouncing, and complete bouncing as function of We^* for sample #2 and sample #4 can be described by a single curve based on the logistic function fitting with $R^2 > 0.97$. For impact outcome of partial bouncing, the deviation between sample #2 and #4 in occurrence proportion is also significantly reduced when plotted against We^* compared to We.

In order to further validate the effectiveness of We^* on describing impact outcomes with different surface properties, extra experiments have been conducted on sample #1, #3, and #5 as presented in Table 3. Four different impact outcome categories from sample #1, #3, and #5 are plotted as function of We^* in the bouncing–wetting transition regime as shown in **Figure 9**. The correlation between impact outcome and We^* is validated by the logistic function derived from sample #2 and #4. It is observed that the occurrence proportion for sample #1, #3, and #5 can be predicted by the logistic function in each impact outcome category with $R^2 > 0.95$ for bouncing and no bouncing category and $R^2 > 0.96$ for the complete bouncing category. The partial bouncing case number on five samples are scattered without a clear trend when plotted as function of We^*, as most impact outcome occurrences for partial bouncing are smaller than 10 which results in a fluctuation in the outcome occurrence. The results suggest that the bouncing and no

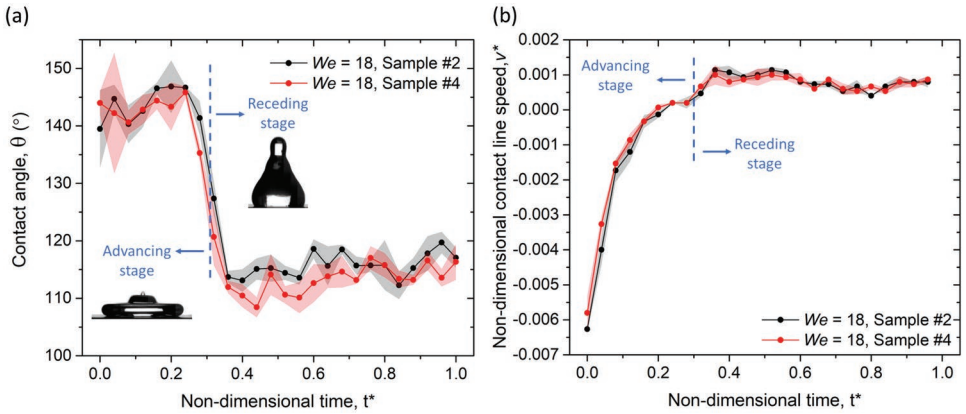

Figure 7. a) Contact angle and b) non-dimensional contact line speed as function of non-dimensional time throughout the droplet impact process. Shaded area refers to standard deviation.

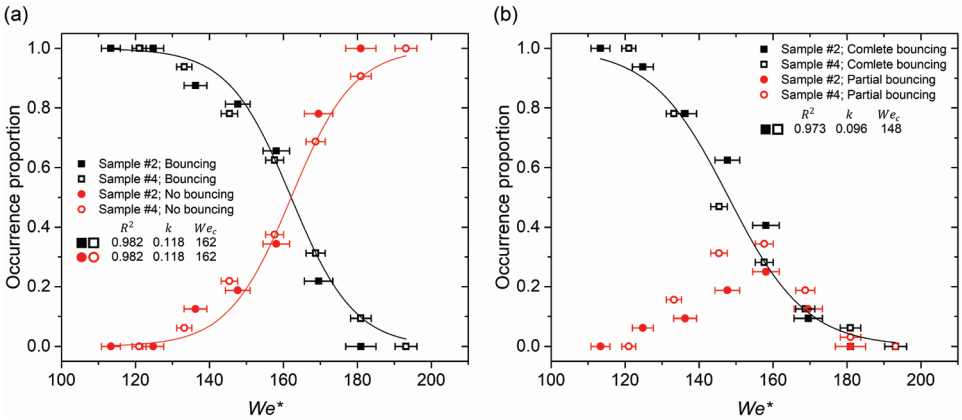

Figure 8. a) Occurrence of bouncing and no bouncing for sample #2 and #4; b) Occurrence of complete bouncing and partial bouncing for sample #2 and #4. All data points are plotted as function of *We**. The error bar derives from the deviation of surface area ratio of different samples.

bouncing impact outcomes on random rough surfaces can be unified by *We** that incorporating the surface area ratio into the original Weber number. The results also further proves that a higher surface area ratio promotes the impact outcome transition from bouncing to no bouncing owning to increased actual surface contact area at the same *We*.

We further analyze the correlation between β and *We** for sample #2 and #4, which give $\beta = 0.57(We^*)^{0.37}$ and $\beta = 0.53(We^*)^{0.38}$, respectively. The results are comparable to the relations derived from Section 3.2, suggesting the effects surface area ratio is neglectable for the droplet spreading factor. In addition to the surface area ratio, RMS roughness is also found to be related to the bouncing–wetting transition behaviors. The surfaces with higher R_q (sample #4) results in a decreased occurrence of bouncing or complete bouncing outcomes compared with surfaces having smaller R_q (sample #2).

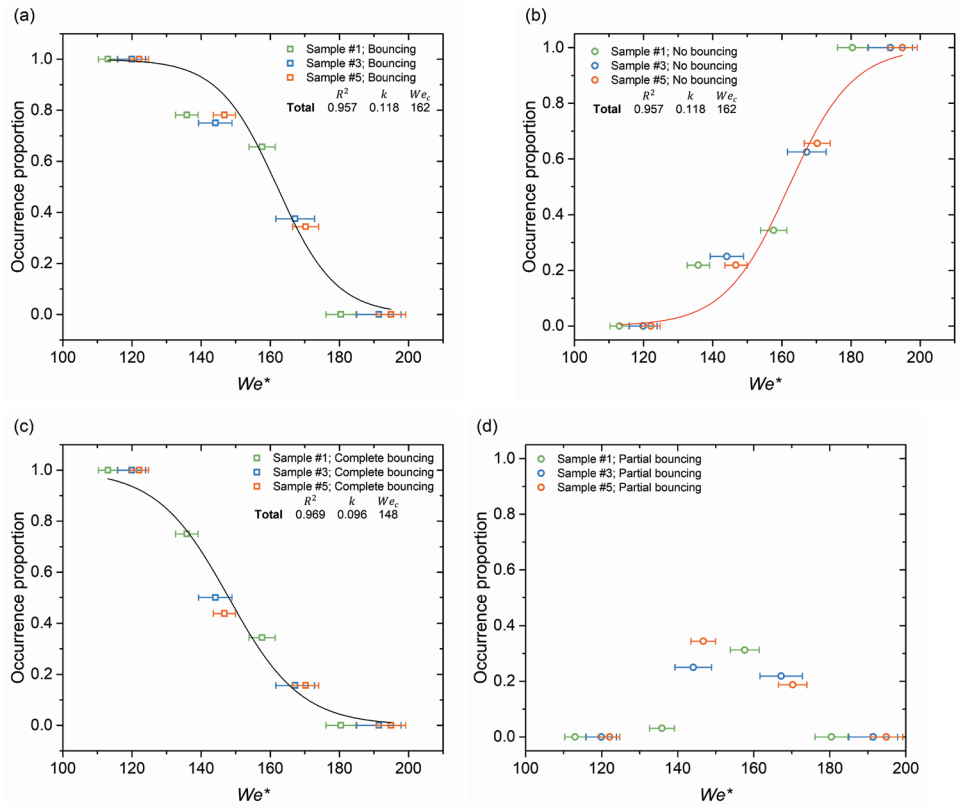

Figure 9. Occurrence proportion on sample #1, #3, and #5 for a) bouncing; b) no bouncing; c) complete bouncing; d) partial bouncing as function of *We**. The logistic function derived from sample #2 and #4 as in Figure 8 is plotted here for comparing additional data except for partial bouncing.

For rough surfaces with random features, various morphological indices can correlate with different measures, e.g., surface area ratio and RMS slope.[50,51] The results qualitatively reported the effects of R_q on droplet bouncing–wetting transition, where higher RMS roughness promotes the transition from bouncing to wetting of impacting droplet. For the roughness slope and fractal dimension, as all five samples have similar roughness slope and fractal dimension, the corresponding effects are not revealed in this study.

4. Conclusion

In this work, we experimentally examined the droplet impact dynamics on PTFE membrane filters, focusing on the influence of surface properties on the droplet bouncing–wetting transition. The surface properties are characterized in terms of surface area, RMS roughness, roughness slope, and fractal dimension. The correlation between maximum spreading factor and *We*/*Re* is presented, showing that kinetic energy is mainly converted to surface energy and viscous dissipation. Six different droplet impact outcomes are revealed, and a transition from bouncing to no bouncing outcome is observed between *We* from 109 to 174. The bouncing–wetting transition is triggered as the increase of *We*, where the adhesion force increases with the droplet maximum spreading factor. In addition, a modified Weber number that considering a combined effect of inertial force, surface tension force, and adhesion force is proposed for the first time to account for the influence of actual surface area on the droplet impact outcomes. We found that the occurrence of droplet impact outcomes in the category of bouncing, no bouncing, and complete bouncing can be described by a single curve as function of *We** with high levels of goodness of fitting. The results suggest that the actual wetted area between droplet and substrate plays an important role in determining the droplet impact outcome on heterogeneous rough surfaces, and a higher surface area ratio promotes the impact outcome transition from bouncing to wetting. RMS roughness of surface is also found to affect the droplet bouncing–wetting transition behaviors, where surfaces with higher RMS roughness have more occurrence of no bouncing outcome. This study provides insights into the effects of surface topological parameters on the droplet impact dynamics, and the results can be served as guidance on surface design for facilitating the droplet nonadhesion feature in varies applications.

Conflict of Interest

The authors declare no conflict of interest.

Data Availability Statement

The data that support the findings of this study are available from the corresponding author upon reasonable request.

Supporting Information

Supporting Information is available from the Wiley Online Library or from the author.

Keywords

adhesion, droplet dynamics, rough interfaces, roughness, surface tension

Received: August 24, 2022
Revised: November 11, 2022
Published online:

[1] M. Pasandideh-Fard, V. Pershin, S. Chandra, J. Mostaghimi, *J. Therm. Spray Technol.* **2002**, *11*, 206.
[2] K. N. Al-Milaji, R. R. Secondo, T. N. Ng, N. Kinsey, H. Zhao, *Adv. Mater. Interfaces* **2018**, *5*, 1701561.
[3] G. Matthews, R. Bateman, P. Miller, *Pesticide Application Methods*, Wiley-Blackwell, Hoboken, NJ, USA **2008**.
[4] S. Pan, N. Wang, D. Xiong, Y. Deng, Y. Shi, *Appl. Surf. Sci.* **2016**, *389*, 547.
[5] A. M. Worthington, *A Study of Splashes*, Longmans, Green, and Company, London **1908**.
[6] C. Josserand, S. T. Thoroddsen, *Annu. Rev. Fluid Mech.* **2016**, *48*, 365.
[7] A. L. Yarin, *Annu. Rev. Fluid Mech.* **2006**, *38*, 159.
[8] Z. Wang, A. Owais, C. Neto, J. M. Pereira, Y. Gan, *Adv. Mater. Interfaces* **2021**, *8*, 2000520.
[9] R. Rioboo, C. Tropea, M. Marengo, *Atomization Sprays* **2001**, *11*, 1.
[10] G. Finotello, R. F. Kooiman, J. T. Padding, K. A. Buist, A. Jongsma, F. Innings, J. Kuipers, *Exp. Fluids* **2018**, *59*, 1.
[11] Z. Wang, W. Qu, J. Xiong, M. Zhong, Y. Yang, *Nucl. Eng. Technol.* **2020**, *52*, 508.
[12] W. Ding, C. A. Dorao, M. Fernandino, *Adv. Mater. Interfaces* **2022**, *9*, 2102564.
[13] J. Hao, S. I. Green, *Phys. Fluids* **2017**, *29*, 012103.
[14] M. Jiang, B. Zhou, *Int. J. Hydrogen Energy* **2020**, *45*, 29848.
[15] B. L. Scheller, D. W. Bousfield, *AIChE J.* **1995**, *41*, 1357.
[16] C. Ukiwe, D. Y. Kwok, *Langmuir* **2005**, *21*, 666.
[17] J. Eggers, M. A. Fontelos, C. Josserand, S. Zaleski, *Phys. Fluids* **2010**, *22*, 062101.
[18] I. V. Roisman, *Phys. Fluids* **2009**, *21*, 052104.
[19] C. Clanet, C. Béguin, D. Richard, D. Quéré, *J. Fluid Mech.* **2004**, *517*, 199.
[20] C. R. Crick, I. P. Parkin, *Chem. - Eur. J.* **2010**, *16*, 3568.
[21] D. Bartolo, F. Bouamrirene, E. Verneuil, A. Buguin, P. Silberzan, S. Moulinet, *EPL - Europhys. Lett.* **2006**, *74*, 299.
[22] E. Bormashenko, *Adv. Colloid Interface Sci.* **2015**, *222*, 92.
[23] Z. Wang, C. Lopez, A. Hirsa, N. Koratkar, *Appl. Phys. Lett.* **2007**, *91*, 023105.
[24] H. Li, K. Zhang, *Appl. Surf. Sci.* **2019**, *498*, 143793.
[25] N. D. Patil, R. Bhardwaj, A. Sharma, *Exp. Therm. Fluid Sci.* **2016**, *74*, 195.
[26] L. K. Malla, N. D. Patil, R. Bhardwaj, A. Neild, *Langmuir* **2017**, *33*, 9620.
[27] D. Hee Kwon, S. J. Lee, *Appl. Phys. Lett.* **2012**, *100*, 171601.
[28] H. Wang, Q. Wu, J. Okagaki, A. Alizadeh, J. A. Shamim, W.-L. Hsu, H. Daiguji, *Int. J. Heat Mass. Transf.* **2021**, *174*, 121304.
[29] T. Deng, K. K. Varanasi, M. Hsu, N. Bhate, C. Keimel, J. Stein, M. Blohm, *Appl. Phys. Lett.* **2009**, *94*, 133109.
[30] S. Mitra, Q. Vo, T. Tran, *Soft Matter* **2021**, *17*, 5969.
[31] S.-C. Zhao, R. de Jong, D. van der Meer, *Phys. Rev. Lett.* **2017**, *118*, 054502.
[32] X. Tang, A. Saha, C. K. Law, C. Sun, *Langmuir* **2018**, *34*, 2654.
[33] J. Hao, *Phys. Fluids* **2017**, *29*, 122105.
[34] T. de Goede, K. de Bruin, N. Shahidzadeh, D. Bonn, *Phys. Rev.* **2021**, *6*, 043604.

[35] A. Latka, A. Strandburg-Peshkin, M. M. Driscoll, C. S. Stevens, S. R. Nagel, *Phys. Rev. Lett.* **2012**, *109*, 054501.
[36] K. Range, F. Feuillebois, *J. Colloid Interface Sci.* **1998**, *203*, 16.
[37] M. A. Quetzeri-Santiago, A. A. Castrejón-Pita, J. R. Castrejón-, *Sci. Rep.* **2019**, *9*, 1.
[38] B. N. Persson, O. Albohr, U. Tartaglino, A. Volokitin, E. Tosatti, *J. Phys.: Condens. Matter* **2004**, *17*, R1.
[39] T. Thomas, *Int. J. Mach. Tools Manuf.* **1998**, *38*, 405.
[40] C. Zhai, Y. Gan, D. Hanaor, G. Proust, D. Retraint, *Exp. Mech.* **2016**, *56*, 359.
[41] X. Wang, C. Zhai, Y. Gan, *Surf. Topogr.: Metrol. Prop.* **2021**, *9*, 025014.
[42] X. Huang, K.-T. Wan, M. E. Taslim, *Phys. Fluids* **2018**, *30*, 094101.
[43] S. Schiaffino, A. A. Sonin, *Phys. Fluids* **1997**, *9*, 3172.
[44] M. Damak, M. N. Hyder, K. K. Varanasi, *Nat. Commun.* **2016**, *7*, 12560.
[45] I. S. Bayer, C. M. Megaridis, *J. Fluid Mech.* **2006**, *558*, 415.
[46] Y. H. Yeong, A. Milionis, E. Loth, I. S. Bayer, *Sci. Rep.* **2015**, *5*, 8384.
[47] M. A. Nilsson, J. P. Rothstein, *J. Colloid Interface Sci.* **2011**, *363*, 646.
[48] Z. Shi, Y. Zhang, M. Liu, D. A. Hanaor, Y. Gan, *Colloids Surf., A* **2018**, *555*, 365.
[49] R. Ford, C. Furmidge, *SCI Monogr.* **1967**, *25*, 417.
[50] R. L. Jackson, Y. Xu, S. Saha, K. D. Schulze, *Fractal Fract.* **2021**, *5*, 44.
[51] B. N. Persson, *J. Chem. Phys.* **2001**, *115*, 3840.